

1 PulseAI: An automated machine learning-based augmentation index detector for arterial  
2 stiffness monitoring from cuff-based measurements

3

4

5 **Authors**

6

7 Alessio Tamborini<sup>1,\*</sup>, Arian Aghilinejad<sup>2</sup>, and Morteza Gharib<sup>1</sup>

8

9 **Affiliations**

10

11 <sup>1</sup>Department of Medical Engineering, California Institute of Technology

12 <sup>2</sup>Department of Bioengineering, University of California, Merced

13

14 **Corresponding Author**

15

16 Alessio Tamborini, [atambori@caltech.edu](mailto:atambori@caltech.edu)

17

18 **Abstract**

19

20 Arterial stiffness is a fundamental characteristic of circulatory physiology and a well-  
21 established predictor of cardiovascular risk and mortality. However, routine clinical  
22 assessment remains limited by the need for dual-site measurements. To address this  
23 challenge, we developed a machine learning algorithm – PulseAI – for automated fiducial  
24 point detection on brachial cuff waveforms for single-site assessment of arterial stiffness.  
25 PulseAI was trained and evaluated using a clinical dataset comprising 5,215 waveforms from  
26 145 heterogeneous subjects. Performance was assessed on fiducial point predictions  
27 accuracy (inflection point,  $t_i$ , and dicrotic notch,  $t_n$ ) and downstream pulse waveform  
28 analysis (PWA) metrics. Our multi-channel convolutional neural network (PulseAI) reported  
29 a median [IQR] on mean absolute error for fiducial point detection of 5 [3, 10] ms. PulseAI  
30 demonstrated high accuracy in predicting  $t_i$  ( $r=0.913$ ,  $p<0.0001$ ) and  $t_n$  ( $r=0.939$ ,  $p<0.0001$ ),  
31 with an average prediction error of 12.6 ms and 6.2 ms for  $t_i$  and  $t_n$ , respectively. While the  $t_n$   
32 results are comparable to other academic models reporting 5-10 ms errors, our approach  
33 provides both fiducial point indices from a single model. PWA features derived from PulseAI  
34 closely matched those derived from human-annotated labels, including systolic pressure-  
35 time integral ( $r=0.988$ ,  $p<0.0001$ ), augmentation index (Alx) ( $r=0.990$ ,  $p<0.0001$ ), and end  
36 systolic pressure ( $r=0.998$ ,  $p<0.0001$ ). Alx tertiles showed statistically significant association  
37 with height-adjusted pulse transit time ( $p<0.05$ ), used as a surrogate of arterial stiffness,  
38 demonstrating the model's sensitivity to stiffness-related changes. These findings  
39 demonstrate that PulseAI enables accurate fiducial point detection and represents a  
40 clinically viable tool for automated, single-site monitoring of arterial stiffness.

41

42

43

44

45 **Keywords**

46

47 Blood pressure; Pulse Waveform Analysis; Machine learning; Augmentation Index; Arterial  
48 Stiffness; Brachial cuff.

49

50 **Highlights**

51

52     • Arterial stiffness is clinically valuable, but complex to assess routinely.

53     • PulseAI reliably detects fiducial points across diverse waveform morphologies.

54     • Spectral machine learning achieves comparable performance with lower

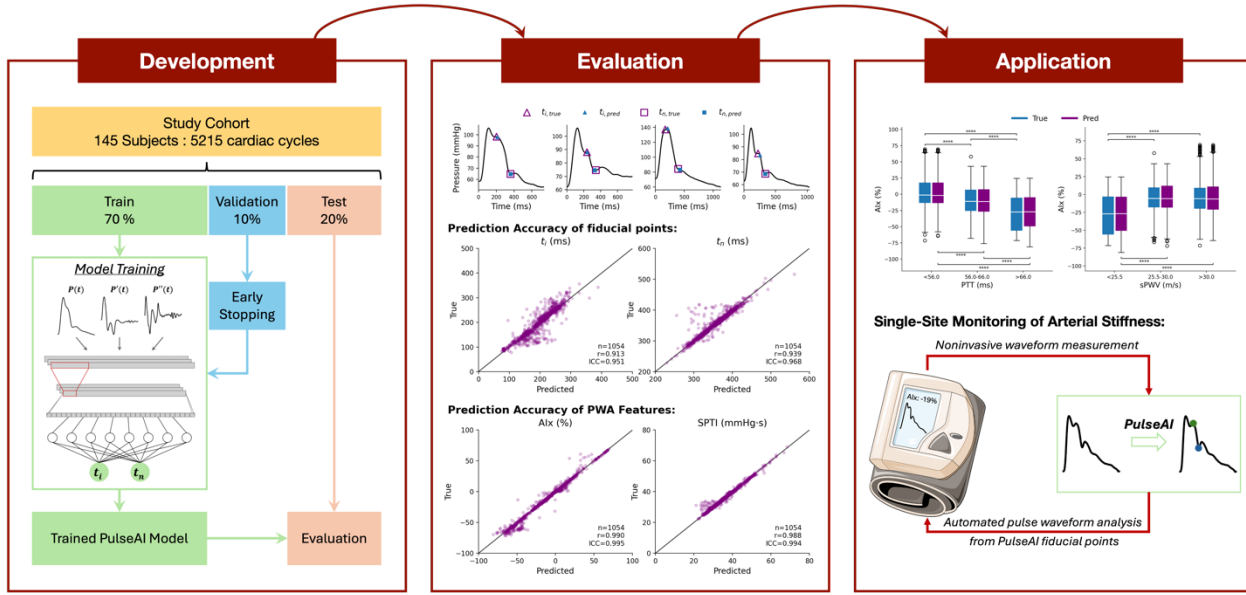
55       complexity.

56     • Alx derived from PulseAI correlates with arterial stiffness assessed via PTT.

57     • PulseAI enables automated, single-site arterial stiffness monitoring.

58

## 59 Graphical Abstract



60

61 **Introduction**

62  
63 Despite significant advances in cardiovascular care, cardiovascular disease (CVD) remains  
64 the leading cause of mortality in developed countries [1]. While blood pressure (BP) is a well-  
65 established risk factor, additional markers have been shown to play a critical role in the  
66 development and progression of CVD [2], [3], [4]. Among these, arterial stiffness has  
67 emerged as an independent predictor of cardiovascular risk and mortality [5], [6]. Large  
68 artery elasticity is a fundamental characteristic of circulatory physiology, helping to buffer  
69 the pulsatile flow generated by cardiac ejection during systole [7]. Pulse wave velocity (PWV)  
70 is a widely recognized metric for assessing arterial stiffness, calculated using the pulse  
71 transit time (PTT) and the propagation distance between two measurement sites [8]. While  
72 PWV is considered the gold standard for arterial stiffness assessment, its reliance on dual-  
73 site measurement introduces practical challenges in clinical settings [9]. On one hand,  
74 efforts have been made to estimate PWV from single-point measurements using machine  
75 learning models, offering a potentially simpler alternative. Jin et al. developed a Gaussian  
76 Process Regression method to estimate PWV from selected waveform features [10]. Mitchell  
77 et al., using a deep learning approach, trained a convolutional neural network (CNN) to  
78 predict carotid-to-femoral PWV from single, uncalibrated waveforms acquired at the radial,  
79 brachial, or femoral sites [11]. Beyond these direct applications, machine learning is being  
80 widely adopted in cardiology for tasks including cardiovascular risk stratification, transfer  
81 functions, and medical image analysis, demonstrating its broad utility [12], [13], [14], [15].  
82 On the other hand, surrogate parameters have been investigated for this purpose.  
83 Augmentation index (Alx) has gained attention as a measure of systemic arterial stiffness  
84 derived from a single cardiac waveform measurement [16]. However, the clinical utility of  
85 such parameters is dependent not only on their theoretical significance but also on the  
86 reliability and precision of their measurement [16], [17], [18].

87  
88 The first key factor influencing this accuracy is the reliability of pulse waveform acquisition.  
89 Increasing attention has been directed toward noninvasive systems such as brachial cuff  
90 devices, due to their ease of use and improved measurement repeatability—both essential  
91 for clinical adoption [19], [20]. In this context, suprasystolic blood pressure (sSBP)  
92 measurements mode have gained prominence for its ability to capture detailed and feature  
93 rich pressure waveforms [19], [21], [22], [15], [23], [14]. Beyond waveform acquisition, the  
94 accurate identification of fiducial points along the cardiac pressure waveform remains a  
95 critical challenge. These points correspond to key physiological events, such as the arrival  
96 of the reflected wave and the closure of the aortic valve, typically marked by the inflection  
97 point and the dicrotic notch, respectively. However, their morphology can vary significantly  
98 depending on the population and study characteristics. For instance, the dicrotic notch may  
99 appear as a distinct physical notch or a subtle incisura, while the inflection point can occur  
100 either before or after the systolic peak. This variability complicates the development of  
101 universally applicable mathematical rules for their detection, often leading researchers to  
102 rely on manual identification or study-specific criteria. For example, Sugawara et al. used  
103 the fourth order derivative to find the systolic inflection point [24], [25], Munir et al. used the  
104 first order derivatives and tangents to determine the location of the inflection point [26], and

105 Ueda et al. used an experienced observer to measure the inflection point [27]. To this end,  
106 several efforts have been dedicated towards developing algorithmic approaches for  
107 automatic identification. Saffarpour et al. developed Physiowise, a physics-aware approach  
108 to dicrotic notch identification [28], Pal et al. pioneered an iterative envelope mean method  
109 for detection of the dicrotic notch [29], [30], and Hoeksel et al. uses a three-element  
110 windkessel model to estimate flow from pressure and then identify the dicrotic notch [31].  
111 While these methods showed promising results, they only focused on a single identification  
112 task and therefore require complementation with other methods for full detection. With the  
113 substantial increment of healthcare dataset size, there is a growing need for  
114 comprehensive, high-precision, and automated tools to facilitate and standardize this  
115 process.

116

117 In this study, we assess the accuracy and generalizability of machine learning for fiducial  
118 point detection, specifically identifying the inflection point and the dicrotic notch, using our  
119 model, PulseAI. We train and evaluate the model on a dataset of manually labeled and  
120 human-annotated cardiac pressure waveforms acquired from a brachial cuff system  
121 operating in sSBP mode [32]. To benchmark its performance, we compare PulseAI's results  
122 against conventional mathematical methods described in the literature and use the 30 ms  
123 reported error ranges as an acceptance criteria [28], [29]. To demonstrate the physiological  
124 relevance of our machine learning pipeline, we have also examined the association between  
125 arterial stiffness and Alx derived from our proposed automated algorithm. Lastly, in order to  
126 provide a standardized and accessible platform for researchers to integrate into their own  
127 studies, the optimized trained model of this study has been made publicly available on  
128 [GitHub](#).

129

## 130 **Methods**

131

### 132 *Clinical Study Design*

133

134 Brachial pressure waveforms were recorded using a custom and laboratory-developed  
135 investigational brachial cuff device designed for high-resolution waveform acquisition [32].  
136 The device has been previously validated against intra-arterial measurements for waveform  
137 accuracy [33]. The device's protocol first performed an oscillometric blood pressure  
138 measurement for calibration, followed by pulse waveform capture using the inflate-and-  
139 hold methodology. This methodology was applied at the sSBP hold, defined as 35 mmHg  
140 above the systolic blood pressure (SBP), and maintained for 40 seconds.

141

142 The dataset analyzed in this study consists of brachial pressure waveforms collected during  
143 cardiac catheterization procedures. Measurements were performed with subjects in the  
144 supine position, and the brachial cuff was placed on the left arm following standard cuff  
145 placement guidelines. The study enrolled individuals aged 21 years or older who were  
146 referred for non-emergent left heart catheterization between September 2021 and  
147 September 2022. Exclusion criteria included recent severe cardiac events (within one  
148 week), inability to undergo routine blood pressure measurement, and contraindications to

149 catheterization. Simultaneous aortic catheterization waveforms were recorded during  
150 brachial cuff measurements to enable PTT calculations. The signals were captured at a  
151 sampling rate of 1 kHz.

152

153 The study was approved by the Institutional Review Board of Western and Salus. Written  
154 informed consent was obtained from all participants before the procedure. The study  
155 adhered to the principles of the Declaration of Helsinki.

156

#### 157 *Study Population*

158

159 The study population included 145 subjects with a mean age of  $66 \pm 9$  years, 88 males (61%),  
160 and a mean body mass index (BMI) of  $29.0 \pm 5.5$  kg/m<sup>2</sup>. Patient characteristics for the entire  
161 study population are summarized in Table 1. The analysis generated a dataset of 5215  
162 waveforms from the brachial cuff during the sSBP hold phase. The distribution of cardiac  
163 cycles per individual showed a median of 37, with interquartile ranges of [30, 43] cycles per  
164 subject, a maximum of 62, and a minimum of 2 (Figure S2). The study population was  
165 partitioned into three cohorts at the subject level using a 70%-10%-20% train-validation-test  
166 split, resulting in cohorts of 102, 14, and 29 subjects, and 3646, 515, and 1054 waveforms,  
167 respectively (Figure 1B). Table S2 provides a summary of the population characteristics for  
168 the training, validation, and test cohorts. Figure S3 shows the cumulative distribution  
169 function of the fiducial points in the time-based format as well as the unit-normalized  
170 configuration; the train-validation-test cohorts showed overlapping distributions for both  $\tilde{t}_i$   
171 and  $\tilde{t}_n$ .

172

#### 173 *Data and Signal Preprocessing*

174

175 The brachial cuff recordings were manually inspected to remove instances of apparatus  
176 malfunction, procedural errors, saturated sensor output, and arrhythmias. The sSBP  
177 pressure signal recordings from the brachial cuff were segmented into individual cardiac  
178 cycles using the foot-to-foot partition method [8]. Each cardiac cycle can be represented  
179 mathematically as,

180

$$181 \quad p_m = p(t_m), \quad m = 0, 1, \dots, N - 1. \quad (1)$$

182

183

184 Where  $N$  is the length of the cardiac cycle. This segmentation resulted in a dataset  
185 containing multiple cardiac cycles for each subject, with each cycle treated as a unique but  
186 dependent data point. While cycles from the same subject were considered distinct, they  
187 were not independent due to the shared underlying physiological characteristics. Fiducial  
188 points of interest on the pressure waveform – namely the peak pressure, inflection point and  
189 dicrotic notch - were manually identified for the entire dataset:

190

191  $t_p = \text{peak time}$

192  $t_i = \text{inflection time}$

193  $t_n = \text{dicrotic notch time}$

194

195 These fiducial points represent key pressure waveform features: peak time corresponds to  
196 maximal systolic pressure, the inflection time marks the arrival of the reflected wave, and  
197 the dicrotic notch time indicates the closure of the aortic valve. The cardiac cycles along with  
198 the fiducial points were combined to generate the dataset for the study.

199

200 Both dataset components – fiducial points and brachial cuff waveforms – were preprocessed  
201 before being fed into the machine learning portion of the study. The fiducial points were  
202 converted to unit-normalized quantities by dividing for the duration of the cardiac cycle,  
203 denoted  $T$ , as shown below:

204

205 
$$\tilde{t}_p = \frac{t_p}{T} ; \quad \tilde{t}_i = \frac{t_i}{T} ; \quad \tilde{t}_n = \frac{t_n}{T} \quad (2)$$

206

207 This normalization ensures that the fiducial points all lie within the range [0,1], which is  
208 optimal for an ML model output.

209

210 Brachial cuff waveforms were individually resampled to a fixed length of 1000 samples to  
211 ensure consistent input size to the ML model. Resampling was performed using a Fourier-  
212 based methodology along the time axis, which is outlined in Algorithm 1. Resampled  
213 waveforms were standardized to a mean value of zero and a standard deviation of one. Upon  
214 performing both procedures, we define these as resampled and normalized waveforms. The  
215 first and second derivatives were computed using the finite difference method on the  
216 resampled and normalized waveforms; interior points were computed with second-order  
217 accurate central differences while at the boundaries we used one-sided differences to  
218 preserve signal length. This signal preprocessing generated a dataset of waveforms – signal,  
219 first derivative and second derivative – with fixed length, centered around zero, and a  
220 standard deviation of one.

221

222

---

**Algorithm 1: Fourier-based Resampling Method**


---

**Input:** waveform signal  $p(t)$ , desired signal length M

**Output:** resampled signal  $p'(t)$

**1. Discrete Fourier Transform**

Convert signal from time domain to frequency domain:

$$P_k = \sum_{m=0}^{N-1} p_m e^{-\frac{j2\pi km}{N}}, \quad k = 0, 1, \dots, N-1.$$

Where  $P_k$  are the frequency components of the original signal, and N is the length of the original signal

**2. Frequency Domain Resampling**

If  $M > N$ , apply zero-padding to the frequency components:

$$P'_k = \begin{cases} P_k, & k = 0, \dots, N/2 \\ 0, & N/2 < k < M - N/2 \\ P_k, & k = M - N/2, \dots, M-1 \end{cases}$$

If  $M < N$ , truncate the frequency components:

$$P'_k = P_k, \quad k = 0, 1, \dots, M-1.$$

**3. Inverse Discrete Fourier Transform**

Convert the signal back to the time domain:

$$p'_j = \frac{1}{M} \sum_{k=0}^{M-1} P'_k e^{-\frac{j\pi kj}{M}}, \quad j = 0, 1, \dots, M-1.$$

225 The dataset was partitioned for standard model training and testing using a 70%-10%-20%  
226 train-validation-test split ratio. Given the dependence of cardiac cycles within a given  
227 subject, the split was performed at the subject level rather than the cardiac cycle level to  
228 prevent data leakage. The training cohort was used for model training, the validation cohort  
229 for early stopping during training, and the testing cohort for model evaluation.

231 *PulseAI Method*

233 The PulseAI method is a machine learning approach developed to identify fiducial points on  
234 the cardiovascular pressure waveform. The model takes as input a single cardiac cycle and  
235 outputs the unit-normalized indices of the fiducial points. In this model implementation, the  
236 PulseAI method was trained to predict the relative time position of the inflection point and  
237 the dicrotic notch for the brachial pressure waveforms in the sSBP hold. Figure 1a shows an  
238 overview of the multi-channel convolutional neural network (CNN) model implemented for  
239 PulseAI. The PulseAI method was optimized for predicting the fiducial points  $t_i$  and  $t_n$

240 through a two-stage process: model architecture evaluation and hyperparameter tuning.  
241 Figure S1 in the supplementary material provides an overview of the optimization approach  
242 used in this study.

243  
244 In the first stage, we evaluated four model architectures: a CNN, a multi-channel CNN  
245 (mcCNN), a multilayer perceptron (MLP), and a Fourier-based Neural Network (fNN). At this  
246 stage, all models used an element-wise mean-square error loss function.

247  
248 The CNN model consisted of three convolutional blocks, each sequentially comprising a 1D  
249 convolutional layer, ReLU activation, and max pooling. The convolutional layers had 8, 16,  
250 and 16 filters, respectively, with a kernel size of 3, a stride of 1, and padding of 1. One-  
251 dimensional max-pooling with a kernel size of 2 and a stride of 2 was applied after each block  
252 to progressively downsample the feature maps. The output of the final convolutional block  
253 was flattened and passed through two fully connected layers: the first with 128 units and the  
254 second mapping to the two output classes. The model processed a single-channel input,  
255 representing the resampled and normalized waveform of length 1000. The mcCNN model  
256 had the same architecture as the CNN model but processed three input channels: the  
257 resampled and normalized waveform, its first derivative, and its second derivative, each of  
258 length 1000. The use of derivatives was intended to capture high-frequency features  
259 embedded within the signal shape.

260  
261 The MLP model consisted of four fully connected layers, mapping an input of 1000 units to  
262 two output units. The three hidden layers contained 128, 64, and 32 units, respectively, each  
263 followed by a ReLU activation function and a dropout rate of 0.35. The fNN model was a fully  
264 connected feedforward neural network operating in the frequency domain. The input signal  
265 was first transformed into the frequency domain, truncated to retain a limited number of  
266 modes, then flattened into its real and imaginary components before being passed into the  
267 network. The network architecture beyond this preprocessing step was identical to the MLP  
268 model. The model architecture that yielded the best performance was selected for  
269 hyperparameter optimization.

270  
271 The hyperparameter tuning phase focused on three key factors: loss function selection, data  
272 augmentation, and regularization. First, we compared model performance with different  
273 base loss functions: mean squared error (MSE), mean absolute error (MAE), and Huber loss  
274 with  $\delta=10$  ms. A penalty term is added to each base loss function making the total loss:

$$\mathcal{L}_{total} = \mathcal{L}_{base} + \mathcal{L}_{penalty} \quad (3)$$

275 The penalty term computes the average of all positive index differences between the  
276 inflection point and dicrotic notch. This penalty effectively enforces the physiological  
277 constraint that the inflection point occurs before the dicrotic notch.

278  
279

$$\mathcal{L}_{penalty} = \frac{1}{n} \sum_{i=1}^n \max(0, \hat{Y}_{i,0} - \hat{Y}_{i,1}) \quad (4)$$

280 Where  $i \in \{1, \dots, n\}$  indexes the samples within the dataset.

281

282

283 Next, we investigated the impact of data augmentation, generating additional training  
284 signals by applying truncation and resampling, and scaling. Three augmentation strategies  
285 were evaluated: (1) truncation and resampling, (2) scaling, and (3) both applied sequentially.  
286 Finally, we explored regularization techniques, testing dropout, weight decay, and their  
287 combined effect. At each step, the best-performing model configuration was carried forward  
288 for further evaluation. This tuning process resulted in nine experimental scenarios, detailed  
289 in Table S1 in the supplementary material. Figure S1 summarizes model selection and  
290 hyperparameter tuning.

291

### 292 *Empirical Method*

293

294 The empirical method served as a reference for comparing model performance in identifying  
295 fiducial points along the pressure waveform. This approach was used to detect both the  
296 inflection point,  $t_i$ , as well as the dicrotic notch,  $t_n$ . The inflection point was determined  
297 using the fourth-order derivative, following the guidelines established by Takazawa et al.  
298 [34]. The dicrotic notch was identified as the first peak of the second derivative occurring  
299 after the minimum of the first derivative, as described by Peter et al. [35] and Takazawa et al.  
300 [36]. The mathematical steps behind the empirical method have been summarized in  
301 Algorithm 2.

302

---

#### **Algorithm 2: Empirical Method for Calculating Fiducial Points**

---

**Input:** waveform signal

**Output:**  $t_b$ ,  $t_i$ ,  $t_n$  (fiducial point indices)

**1. Compute Derivatives:**

- 1.1.  $p(t)_{d1} \leftarrow \nabla p(t)$  (*first derivative*)
- 1.2.  $p(t)_{d2} \leftarrow \nabla p(t)_{d1}$  (*second derivative*)
- 1.3.  $p(t)_{d3} \leftarrow \nabla p(t)_{d2}$  (*third derivative*)
- 1.4.  $p(t)_{d4} \leftarrow \nabla p(t)_{d3}$  (*fourth derivative*)

**2. Identify Maximum Value:**

- 2.1.  $t_p \leftarrow \arg \max (p(t))$

**3. Determine Slope at Maximum:**

- 3.1.  $slope_{d4} \leftarrow p(t_{max})_{d4}$

---

---

**4. Identify Inflection Point:**

**If**  $slope_{d4} > 0$  (*late systolic peak*):

4.1. Identify zero-crossings of  $p(t)_{d4}$  (*positive to negative*)

**If** at least two zero-crossings exist before  $t_p$ :

o  $t_i \leftarrow$  second zero-crossing of  $p(t)_{d4}$

**Else:**

o  $t_i \leftarrow$  None

**Else** (*early systolic peak*):

4.2. Identify zero-crossings of  $p(t)_{d4}$  (*negative to positive*)

**If** at least three zero-crossings exist after  $t_p$ :

o  $t_i \leftarrow$  third zero-crossing of  $p(t)_{d4}$

**Else:**

o  $t_i \leftarrow$  None

**5. Identify Dicrotic Notch:**

5.1.  $t_{d1,min} \leftarrow \arg \min(p(t)_{d1})$

5.2.  $t_n \leftarrow \arg \max(p(t_{d1,min}:)_{d2}) + t_{d1,min}$

**6. Return:**  $(t_p, t_i, t_n)$ 

---

303304 *Hemodynamic Analyses*

305

306 Pressure waveforms captured with a brachial cuff system are in non-physiological units, as  
307 they represent the pressure fluctuations inside the cuff. To convert these waveforms into  
308 physiological units, we applied a previously validated calibration procedure using the blood  
309 pressure values from the oscillometric measurement [33]. The waveforms were scaled such  
310 that the peak pressure corresponds to SBP, and the base pressure corresponds to diastolic  
311 blood pressure (DBP). The calibration equation used is:

312

$$313 p_{calib} = \frac{p(t) - \min(p(t))}{\max(p(t)) - \min(p(t))} * (SBP - DBP) + DBP \quad (5)$$

314

315

316 Where  $p_{calib}$  represents the calibrated pressure waveform.

317

318 Pulse wave analysis (PWA) was performed on the calibrated waveform to extract clinically  
319 significant parameters, including Alx, systolic pressure time integral (SPTI), and end-systolic  
320 pressure (ESP). These parameters were computed using both the measured (human-  
321 annotated) and PulseAI-generated fiducial points. Additionally, PTT—the foot-to-foot time  
322 difference between the start of the waveform at the central site (captured via catheter) and  
323 cuff waveforms—was calculated in milliseconds. PTT was further adjusted for subject height  
324 to derive a surrogate measure of PWV, herein denoted as sPWV, both of which serve as  
325 indicators of arterial stiffness [8].

326

328

$$AIx = \begin{cases} \frac{p(t_p) - p(t_i)}{p(t_p) - p(t_0)}, & \text{if } t_i < t_p \\ \frac{p(t_i) - p(t_p)}{p(t_p) - p(t_0)}, & \text{otherwise} \end{cases} \quad (6)$$

327

330

$$SPTI = \int_{t_0}^{t_n} p(t) dt \quad (7)$$

329

331

$$ESP = p(t_n) \quad (8)$$

332

333

$$PTT = t_{foot,cath} - t_{foot,cuff} \quad (9)$$

334

335

$$sPWV = \frac{Height}{PTT} \quad (10)$$

336

337

### 338 Statistical Analyses

339

340 Fiducial point prediction accuracy was evaluated in the time domain. To recover the  
 341 predicted fiducial point values, the unit-normalized predictions were multiplied by the  
 342 cardiac cycle duration and rounded to the nearest millisecond (ms). Model performance was  
 343 assessed by calculating the prediction error (true – predicted) for individual fiducial points,  
 344 as well as the mean absolute error (MAE) for joint predictions. Several metrics were used to  
 345 evaluate model accuracy, including the Pearson correlation coefficient (r), coefficient of  
 346 determination ( $R^2$ ), root mean squared error (RMSE), mean difference, and limits of  
 347 agreement. The prediction accuracy for fiducial points and PWA-derived parameters was  
 348 visualized using scatter plots of true-versus-predicted values and Bland-Altman analysis.  
 349 Correlation strength was quantified using r and the intraclass correlation coefficient (ICC),  
 350 along with 95% confidence intervals (95% CI). Bland-Altman analysis was also used to  
 351 assess bias and limits of agreement. Significance level was set at a value of  $p < 0.05$ .

352

353

## 354 Results

355

### 356 Model Development

357

358 The PulseAI model was trained on the training cohort (3,646 cardiac cycles) with an early  
 359 stopping criterion based on the validation cohort (515 cardiac cycles) and evaluated on the  
 360 testing cohort (1,054 cardiac cycles). Model architecture optimization, summarized in Figure  
 361 2 and Table S3, was performed across four different model configurations and the empirical  
 362 method. The mcCNN model demonstrated the highest fiducial point prediction accuracy,  
 363 with a median [IQR] error (true - predicted) of 0 [-7, 7.75] ms for  $t_i$  and 1 [-3, 4] ms for  $t_n$ . The

364 fNN model had the second-best performance, with a median [IQR] error of -3 [-17, 13] ms for  
365  $t_i$  and -1 [-7, 6] ms for  $t_n$ . The combined MAE for fiducial point prediction was lowest for the  
366 mcCNN model (median [IQR] = 6 [3, 12.5] ms) and highest for the empirical method (median  
367 [IQR] = 73 [56, 96.5] ms). Both the mcCNN and fNN models significantly outperformed the  
368 other models in predicting  $t_i$  and  $t_n$  as measured with  $r$  and  $R^2$ , as shown in Table S2. The  
369 algorithms were tested with cross-validation on incremental relative training sizes, the fNN  
370 and mcCNN significantly outperformed the other models across all training sizes (Figure S4).  
371 Based on these results, the mcCNN architecture was selected for further tuning.

372  
373 Hyperparameter tuning was performed sequentially to explore potential improvements in  
374 model performance. Three sets of experiments were conducted to evaluate the loss function  
375 (experiments #1–3), data augmentation strategies (experiments #4–6), and regularization  
376 methods (experiments #7–9). The first set of experiments (#1–3) indicated that the MAE base  
377 loss function produced the most accurate predictions for  $t_i$  ( $r=0.88$ ,  $R^2=0.77$ , RMSE=25ms)  
378 and  $t_n$  ( $r=0.91$ ,  $R^2=0.82$ , RMSE=17ms), leading to its selection for subsequent experiments.  
379 The second set (#4–6) tested different data augmentation techniques. The truncate and  
380 resample method (experiment #4) yielded the best improvement for  $t_i$  prediction ( $r=0.92$ ,  
381  $R^2=0.85$ , RMSE=21ms), while the combination of truncation and resampling, and scaling  
382 (experiment #6) provided the highest accuracy for  $t_n$  ( $r=0.94$ ,  $R^2=0.88$ , RMSE=14ms). Since  
383 the performance difference between experiments #4 and #6 for  $t_i$  was minimal, the  
384 configuration from experiment #6 was chosen for further testing. Finally, experiments #7–9  
385 assessed different regularization techniques, but none resulted in improved prediction  
386 accuracy. A summary of the hyperparameter tuning results is provided in Table 2 and Figure  
387 S5 in the supplementary material. Based on these findings, the final model configuration  
388 was selected from experiment #6. This corresponds to the mcCNN architecture with an MAE  
389 base loss function and data augmentation using both the truncate and resample method  
390 along with scaling. Specifically, the mcCNN model takes three channels as inputs –  
391 waveform, first and second derivative – and has three convolutional blocks followed by fully  
392 connected layers. The convolutional blocks are each made up of a 1D convolutional layer, a  
393 ReLU activation and a max pooling step; convolutional layers have 8, 16, and 16 dimensions,  
394 a kernel size of 3, and a stride and padding of 1. The fully connected layers convert feature  
395 maps to the fiducial point indices; the first layer is a dense layer with 128 units and ReLU  
396 activation and the output layer has 2 units.

397

### 398 *Model Evaluation*

399

400 The PulseAI model, incorporating the mcCNN architecture, MAE loss function, and selected  
401 data augmentation strategies, was evaluated on the test cohort (1,054 cardiac cycles).  
402 Figure 3A presents the model's mean absolute error distribution, with a median [IQR] error  
403 of 5 [3, 10] ms. Figure 3B visualizes the positioning of true versus predicted fiducial points ( $t_i$   
404 and  $t_n$ ) across the entire error spectrum. The model reported an average MAE of 9.4 ms with  
405 a 95% confidence interval of [8.6, 10.1] and an average RMSE of 18.1 ms with a confidence  
406 interval of [17.3, 19.0]. Figure 4 illustrates the prediction accuracy for fiducial points using  
407 true-versus-predicted plots and Bland-Altman analysis. The  $t_i$  point demonstrated a strong

408 linear correlation ( $r=0.913$ ,  $p<0.0001$ ;  $ICC=0.951$ ) with no bias ( $B$  [LOA] = 0 [-42, 43] ms).  
409 Similarly, the  $t_n$  point exhibited a strong linear correlation ( $r=0.939$ ,  $p<0.0001$ ;  $ICC=0.958$ ),  
410 with no observed bias ( $B$  [LOA] = 0 [-27, 27] ms). The average error in fiducial point  
411 identification was below the permitted error range of 30 ms for both  $t_i$  (12.6 ms) and  $t_n$  (6.2  
412 ms). A stratified analysis of the PulseAI model performance with the mcCNN architecture  
413 was performed for age, gender, and hypertensive status, results summarized in Table S4.  
414 Figure 5 qualitatively demonstrates that prediction accuracy is consistent across the three  
415 pressure waveform types—Type A, Type B, and Type C—classified based on Alx.  
416

#### 417 *Physiological relevancy of the Approach*

418

419 The true and predicted fiducial points were used to extract clinically relevant features from  
420 the cardiac pressure waveform via PWA. Figure 6 compares PWA accuracy using PulseAI-  
421 predicted fiducial points versus true measurements (human-annotated) for Alx, SPTI, and  
422 ESP. Alx exhibited a strong correlation between predicted and true values ( $r=0.990$ ,  
423  $p<0.0001$ ;  $ICC=0.995$ ) with no detectable bias ( $B$  [LOA] = 0 [-9, 8] %). Similarly, SPTI  
424 demonstrated high agreement ( $r=0.988$ ,  $p<0.0001$ ;  $ICC=0.994$ ) with negligible bias ( $B$  [LOA]  
425 = 0.0 [-2.1, 2.1] %). ESP also showed excellent concordance ( $r=0.998$ ,  $p<0.001$ ;  $ICC=0.999$ )  
426 and minimal bias ( $B$  [LOA] = -0.2 [-1.4, 1.1] mmHg).  
427

428

429 Alx values, computed using both true and predicted fiducial points, were further analyzed in  
430 relation to arterial stiffness metrics, specifically PTT (in milliseconds) and sPWV (in meters  
431 per second) (Figure 7). Three instances with non-physiological negative PTT values were  
432 excluded. A tertile analysis of PTT classified the population into three subgroups: T1 (n=362)  
433 with (8, 56] ms, T2 (n=368) with (56, 66] ms, and T3 (n=321) with (66, 85] ms. Alx  
434 demonstrated a clear inverse relationship with PTT, with significant differences observed  
435 between all tertiles (T1 vs. T2, T2 vs. T3, and T1 vs. T3; all  $p<0.05$ ). Additionally, no significant  
436 differences were found between true and predicted Alx values within each tertile group (all  
437  $p > 0.05$ ).  
438

439

440 A similar tertile analysis was conducted for sPWV, dividing the population into T1 (n=351)  
441 with (19, 25.5] m/s, T2 (n=362) with (25.5, 30] m/s, and T3 (n=338) with (30, 210] m/s. Alx  
442 exhibited a positive correlation with sPWV, with significant differences found between T1 and  
443 T2 as well as between T1 and T3 (both  $p < 0.05$ ), though no statistical difference was  
444 observed between T2 and T3 ( $p > 0.05$ ). Also, for sPWV no significant differences were  
445 detected between true and predicted Alx values across all tertile groups (all  $p > 0.05$ ).  
446

447

448

449

450

451

## 452 **Discussion**

453

454

455

456

457

458

459

460

461

462

463

464

465

466

467

468

469

470

471

472

473

474

475

476

477

478

479

480

481

482

483

484

485

486

487

488

489

490

491

492

493

494

495

496

497

498

499

500

501

502

503

504

505

506

507

508

509

510

511

512

513

514

515

516

517

518

519

520

521

522

523

524

525

526

527

528

529

530

531

532

533

534

535

536

537

538

539

540

541

542

543

544

545

546

547

548

549

550

551

552

553

554

555

556

557

558

559

560

561

562

563

564

565

566

567

568

569

570

571

572

573

574

575

576

577

578

579

580

581

582

583

584

585

586

587

588

589

590

591

592

593

594

595

596

597

598

599

600

601

602

603

604

605

606

607

608

609

610

611

612

613

614

615

616

617

618

619

620

621

622

623

624

625

626

627

628

629

630

631

632

633

634

635

636

637

638

639

640

641

642

643

644

645

646

647

648

649

650

651

652

653

654

655

656

657

658

659

660

661

662

663

664

665

666

667

668

669

670

671

672

673

674

675

676

677

678

679

680

681

682

683

684

685

686

687

688

689

690

691

692

693

694

695

696

697

698

699

700

701

702

703

704

705

706

707

708

709

710

711

712

713

714

715

716

717

718

719

720

721

722

723

452 challenging to define. This challenge is further amplified in noninvasive signals, where high-  
453 frequency components tend to be attenuated, making these features less distinct. In the  
454 literature, there are several mathematical definitions used for the identification of these  
455 points [35], [38]. For example, Takazawa et al. used a conditional definition based on the  
456 fourth-order pressure derivative to determine whether the inflection point occurs before or  
457 after the systolic peak, followed by zero crossings to determine its precise location [34].  
458 Other studies have used second order derivative crossings [36], while others have identified  
459 this point based on the intersection of tangents drawn at local minima and maxima in the  
460 waveform's first derivative [26]. Similar trends can be observed for the identification of the  
461 dicrotic notch. While the notch is easily defined when distinctly visible, its definition can  
462 become ambiguous in cases where it is represented by an incisura, making its identification  
463 reliant on higher-order derivative behaviors [39], [40], [41], [42], [43]. Moreover, the diversity  
464 in waveform morphologies may necessitate different identification strategies to ensure  
465 accurate detection across various patient populations and physiological conditions.  
466 Although these features are often easily identifiable by visual inspection from a trained  
467 individual, translating their characteristics into precise mathematical definitions is a  
468 complex task. This inherent complexity makes fiducial point detection particularly well-  
469 suited for machine learning-based pattern recognition approaches, which can effectively  
470 capture subtle waveform variations and improve detection robustness.

471  
472 In this study, we evaluated multiple model architectures and preprocessing strategies to  
473 identify the optimal approach for fiducial point detection. Among the four tested  
474 architectures, the mcCNN demonstrated the lowest prediction error. This model processes  
475 the pressure signal along with its first and second derivatives to identify fiducial points,  
476 significantly outperforming the single-channel CNN model in terms of MAE ( $p < 0.05$ ). This  
477 improvement suggests that incorporating the pressure signal's derivatives provided  
478 additional valuable information for the pattern recognition task. Interestingly, this result  
479 aligns with empirical strategies commonly described in the literature, where higher-order  
480 derivatives are employed to identify these fiducial points as signal characteristics are more  
481 apparent [34], [36]. Given that CNN models rely on filters to extract patterns from signals,  
482 this additional information from the waveform derivatives appears to enhance model  
483 performance effectively.

484  
485 As part of the model comparison, we also assessed the performance of an empirical method  
486 based on conventional definitions of fiducial points found in the literature [34], [43]. As  
487 shown in Figure 2 and Table S3 in the supplementary material, the machine learning models  
488 strongly outperformed the empirical method. The prediction of the inflection point,  $t_i$ ,  
489 exhibited a wide error distribution, with interquartile ranges between -74 to 137 ms. This  
490 suggests that the empirical method frequently misidentified early systolic peaks as late  
491 systolic peaks, or vice versa, highlighting the difficulty in defining mathematical rules to  
492 classify such points. Another notable observation from this analysis is that the fNN method  
493 achieved only slightly lower performance than the mcCNN (mcCNN MAE = 6 ms; fNN MAE =  
494 12.5 ms), while maintaining a substantially smaller model size (mcCNN = 257k parameters;  
495 fNN = 15.5K parameters). Although the mcCNN model was chosen for downstream analysis

496 due to superior performance, these results highlight the effectiveness of spectral machine  
497 learning in developing compact yet accurate models [15], [44], [45].

498  
499 Our findings further demonstrated that preprocessing strategies applied to the mcCNN  
500 model improved performance. The most notable improvement resulted from the data  
501 augmentation strategy, which involved modifying the input data such that a single data point  
502 was used multiple times in the training set with different configurations. The base dataset  
503 preprocessing included normalizing all input waveforms to a uniform length of 1000 units  
504 and standardizing the amplitude to have zero mean and unit standard deviation. Two data  
505 augmentation strategies were then applied: (1) rescaling the waveform amplitudes and (2)  
506 truncating and resampling the waveforms. Since the inflection point and dicrotic notch  
507 follow physiological phenomena, they tend to occur in relatively consistent locations.  
508 Truncating and resampling shifted the location of these fiducial points within the waveform  
509 while preserving its key features. This strategy aimed to prevent the model from learning a  
510 fixed positional bias and instead focus on recognizing signal-based characteristics.  
511 Similarly, rescaling the waveform amplitude was designed to prevent the model from relying  
512 on amplitude patterns and instead promote recognition of relevant waveform features.  
513 Conceptually, these data augmentation strategies were intended to expand the effective  
514 size of the training dataset by allowing a single real data point to contribute multiple useful  
515 and non-redundant samples. This is particularly important in clinical data applications,  
516 where data collection is often challenging and time-consuming. By engineering effective  
517 augmentation techniques, we can maximize the utility of available data and improve model  
518 robustness in real-world scenarios.

519  
520 The variability in waveform morphology is highly prevalent in noninvasive datasets, making  
521 it crucial for the model to generalize across the entire spectrum. To assess this, we first  
522 examined how prediction errors translated to the physical placement of fiducial points. As  
523 shown in Figure 3B, across the MAE spectrum—from the 5th percentile to the 95th  
524 percentile—the placement of fiducial points remained well-preserved. We further  
525 investigated how the model’s predictions varied with waveform morphology, measured  
526 using the Alx as defined by Murgo et al. [46]. As shown in Figure 5, the model accurately  
527 identified fiducial points across the full spectrum of waveform morphologies—Type A, B, and  
528 C—correctly distinguishing early and late systolic peaks and appropriately placing the  
529 dicrotic notch, whether represented by a distinct notch or an incisura. These results  
530 demonstrate the model’s strong generalizability to waveforms with diverse morphologies,  
531 which are commonly encountered in clinical measurements.

532  
533 Accurate fiducial point detection is crucial for consistent PWA. While our detection method  
534 introduces minimal error (MAE = 5 ms), the error is sufficiently small to ensure a strong one-  
535 to-one correlation between waveform parameters measured using predicted fiducial points  
536 and those measured with human-annotated points (Alx  $R^2=0.980$ ; SPTI  $R^2=0.975$ ; ESP  
537  $R^2=0.998$ ). This level of precision is particularly important, as PWA is widely getting popular  
538 in both research and clinical settings to extract valuable information from pressure  
539 waveforms and aid in diagnostic assessments [16], [47], [48], [49], [50]. Arterial stiffness is

540 an established independent predictor of adverse cardiovascular events and PWA is a key  
541 method for assessing this parameter [51], [52], [53], [54]. Alx is closely linked to arterial  
542 properties, particularly through variations in pulse wave velocity and wave arrival time. As  
543 arterial stiffness increases, the pulse wave travels faster, causing the reflected wave from  
544 peripheral sites to return earlier during systole [55]. This premature arrival amplifies systolic  
545 pressure, thereby increasing left ventricular afterload [55]. In this study, we demonstrated  
546 the inverse relationship between Alx and PTT – the time of pressure wave propagation  
547 between two points along the arterial system [56]. Additionally, our findings demonstrate  
548 that a longer transit time reduces the reflected wave contribution to afterload, as measured  
549 by lower Alx values. Given that Alx is highly dependent on the precise and consistent  
550 identification of the waveform's inflection point [57], our results further highlight the critical  
551 role of accurate fiducial point detection for ensuring reliable PWA measurements. Therefore,  
552 we envision that PulseAI could be directly integrated into PWA of cardiac pressure waveform  
553 to perform single-site monitoring of arterial stiffness via Alx.

554

555 This study and its models have some limitations. First, the models were trained only on  
556 waveforms from a brachial cuff system in sSBP hold. Since pressure waveform morphology  
557 varies throughout the arterial tree, these models may not perform optimally on waveforms  
558 from different measurement sites or modalities. Expanding the training dataset to include  
559 diverse waveform sources is essential for broader applicability. Another limitation is the  
560 trade-off between generalizability and accuracy. While our ML model effectively handles  
561 diverse waveform morphologies, this flexibility may reduce precision in highly consistent  
562 waveform patterns. In such cases, empirical methods may outperform the model, as they  
563 can achieve near-perfect accuracy when waveform characteristics are stable and well-  
564 defined. However, in real-world clinical data, where waveform variability is common, our  
565 model's adaptability is key to ensuring reliable performance across different patient profiles  
566 and conditions. Lastly, we acknowledge the ongoing debate in the literature regarding the  
567 use of Alx to assess arterial stiffness. At the level of wave dynamics, Alx is governed by  
568 arterial wave reflections and vascular properties, however several physiological factors  
569 strongly modulate this relationship. As such, some studies have reported weak or  
570 inconsistent associations between Alx and arterial stiffness [58], [59], [60]. While this study  
571 is motivated by the clinical relevance of Alx, we recognize that Alx might not always serve as  
572 a standalone assessment of arterial stiffness.

573

574

## 575 **Conclusion**

576

577 Our study developed and validated the PulseAI method for identifying  $t_i$  and  $t_n$  on a cardiac  
578 waveform to serve as a tool for monitoring arterial stiffness from single-site pressure  
579 measurements. PulseAI was trained to predict the location of fiducial points from resampled  
580 and standardized pressure waveforms measured using a brachial cuff in the sSBP hold. The  
581 optimized model demonstrated strong predictive accuracy, achieving a MAE of 9.4 ms  
582 overall, with errors of 12.6 ms for  $t_i$  and of 6.2 ms for  $t_n$ , both of which fall within the  
583 acceptance error range of 30ms. Accurate fiducial point detection is the foundation for

584 reliable PWA, which enabled precise measurements of Alx, SPTI, and ESP using the  
585 predicted fiducial points. Alx from the brachial waveform revealed an inverse relationship  
586 with PTT, a surrogate metric of PWV, consistent with established arterial stiffness metrics.  
587 These results highlighted that Alx measured at the brachial is sensitive to elevated arterial  
588 stiffness. In conclusion, this study demonstrated that machine learning-based fiducial point  
589 detection provides a reliable approach for accurate PWA and a practical tool for single-site  
590 assessment of arterial stiffness-related metrics.

591

592 **Acknowledgements**  
593  
594 Part of figure 1 and the Graphical Abstract were generated with adapted illustrations from  
595 Servier Medical Art, provided by Servier and licensed under a Creative Commons  
596 Attribution 3.0 Unported License.  
597  
598  
599 **Data Availability**  
600  
601 Data were obtained from a data transfer and use agreement between Caltech and Avicena  
602 LLC (d.b.a. Ventric Health).  
603  
604  
605 **Declaration of Competing Interests**  
606  
607 AT is a consultant for Avicena LLC but declares no non-financial competing interests. MG is  
608 a co-founder of Avicena LLC but declares no non-financial competing interests. All other  
609 authors declare no financial and non-financial competing interests.  
610  
611  
612 **Declaration of generative AI and AI-assisted technologies in the manuscript**  
613 **preparation process**  
614  
615 During the preparation of this work the author(s) used ChatGPT for proofreading and editing  
616 purposes. After using this tool/service, the author(s) reviewed and edited the content as  
617 needed and take(s) full responsibility for the scientific content and accuracy of the  
618 published article.  
619  
620 **References**  
621  
622 [1] S. S. Martin *et al.*, “2024 Heart Disease and Stroke Statistics: A Report of US and Global  
623 Data From the American Heart Association,” *Circulation*, vol. 149, no. 8, Feb. 2024, doi:  
624 10.1161/CIR.0000000000001209.  
625 [2] S. Laurent *et al.*, “Aortic Stiffness Is an Independent Predictor of All-Cause and  
626 Cardiovascular Mortality in Hypertensive Patients,” *Hypertension*, vol. 37, no. 5, pp.  
627 1236–1241, May 2001, doi: 10.1161/01.HYP.37.5.1236.  
628 [3] J. He and P. K. Whelton, “Elevated systolic blood pressure and risk of cardiovascular  
629 and renal disease: overview of evidence from observational epidemiologic studies and  
630 randomized controlled trials,” *Am Heart J*, vol. 138, no. 3 Pt 2, pp. 211–219, Sep. 1999,  
631 doi: 10.1016/s0002-8703(99)70312-1.  
632 [4] K. Sutton-Tyrrell *et al.*, “Elevated Aortic Pulse Wave Velocity, a Marker of Arterial  
633 Stiffness, Predicts Cardiovascular Events in Well-Functioning Older Adults,”  
634 *Circulation*, vol. 111, no. 25, pp. 3384–3390, Jun. 2005, doi:  
635 10.1161/CIRCULATIONAHA.104.483628.

636 [5] P. Boutouyrie, P. Chowienczyk, J. D. Humphrey, and G. F. Mitchell, "Arterial Stiffness and  
637 Cardiovascular Risk in Hypertension," *Circulation Research*, vol. 128, no. 7, pp. 864–  
638 886, Apr. 2021, doi: 10.1161/CIRCRESAHA.121.318061.

639 [6] G. F. Mitchell *et al.*, "Arterial Stiffness and Cardiovascular Events," *Circulation*, vol. 121,  
640 no. 4, pp. 505–511, Feb. 2010, doi: 10.1161/CIRCULATIONAHA.109.886655.

641 [7] J. P. Merillon, G. Motte, J. Fruchaud, C. Masquet, and R. Gourgon, "Evaluation of the  
642 elasticity and characteristic impedance of the ascending aorta in man," *Cardiovasc  
643 Res*, vol. 12, no. 7, pp. 401–406, Jul. 1978, doi: 10.1093/cvr/12.7.401.

644 [8] R. Asmar *et al.*, "Assessment of Arterial Distensibility by Automatic Pulse Wave Velocity  
645 Measurement," *Hypertension*, vol. 26, no. 3, pp. 485–490, Sep. 1995, doi:  
646 10.1161/01.HYP.26.3.485.

647 [9] I. B. Wilkinson, K. M. Mäki-Petäjä, and G. F. Mitchell, "Uses of Arterial Stiffness in  
648 Clinical Practice," *Arteriosclerosis, Thrombosis, and Vascular Biology*, vol. 40, no. 5, pp.  
649 1063–1067, May 2020, doi: 10.1161/ATVBAHA.120.313130.

650 [10] W. Jin, P. Chowienczyk, and J. Alastruey, "Estimating pulse wave velocity from the  
651 radial pressure wave using machine learning algorithms," *PLOS ONE*, vol. 16, no. 6, p.  
652 e0245026, Jun. 2021, doi: 10.1371/journal.pone.0245026.

653 [11] G. F. Mitchell *et al.*, "Vascular Age Assessed From an Uncalibrated, Noninvasive  
654 Pressure Waveform by Using a Deep Learning Approach: The AI-VascularAge Model,"  
655 *Hypertension*, vol. 81, no. 1, pp. 193–201, Jan. 2024, doi:  
656 10.1161/HYPERTENSIONAHA.123.21638.

657 [12] S. J. Al'Aref *et al.*, "Clinical applications of machine learning in cardiovascular  
658 disease and its relevance to cardiac imaging," *Eur Heart J*, vol. 40, no. 24, pp. 1975–  
659 1986, Jun. 2019, doi: 10.1093/eurheartj/ehy404.

660 [13] C. Krittawong *et al.*, "Machine learning prediction in cardiovascular diseases: a  
661 meta-analysis," *Sci Rep*, vol. 10, no. 1, p. 16057, Sep. 2020, doi: 10.1038/s41598-020-  
662 72685-1.

663 [14] A. Tamborini, A. Aghilinejad, R. V. Matthews, and M. Gharib, "Machine Learning  
664 Reconstruction of Left Ventricular Pressure From Peripheral Waveforms," *JACC:  
665 Advances*, vol. 4, no. 9, p. 102104, Sep. 2025, doi: 10.1016/j.jacadv.2025.102104.

666 [15] A. Tamborini, A. Aghilinejad, and M. Gharib, "A spectral machine learning approach  
667 to derive central aortic pressure waveforms from a brachial cuff," *Proc. Natl. Acad. Sci.  
668 U.S.A.*, vol. 122, no. 9, p. e2416006122, Mar. 2025, doi: 10.1073/pnas.2416006122.

669 [16] I. B. Wilkinson, H. MacCallum, L. Flint, J. R. Cockcroft, D. E. Newby, and D. J. Webb,  
670 "The influence of heart rate on augmentation index and central arterial pressure in  
671 humans," *J Physiol*, vol. 525, no. Pt 1, pp. 263–270, May 2000, doi: 10.1111/j.1469-  
672 7793.2000.t01-1-00263.x.

673 [17] C.-H. Chen *et al.*, "Estimation of Central Aortic Pressure Waveform by Mathematical  
674 Transformation of Radial Tonometry Pressure," *Circulation*, vol. 95, no. 7, pp. 1827–  
675 1836, Apr. 1997, doi: 10.1161/01.CIR.95.7.1827.

676 [18] J. E. Sharman, J. E. Davies, C. Jenkins, and T. H. Marwick, "Augmentation Index, Left  
677 Ventricular Contractility, and Wave Reflection," *Hypertension*, vol. 54, no. 5, pp. 1099–  
678 1105, Nov. 2009, doi: 10.1161/HYPERTENSIONAHA.109.133066.

679 [19] B. T. Costello, M. G. Schultz, J. A. Black, and J. E. Sharman, “Evaluation of a Brachial  
680 Cuff and Suprasystolic Waveform Algorithm Method to Noninvasively Derive Central  
681 Blood Pressure,” *Am J Hypertens*, vol. 28, no. 4, pp. 480–486, Apr. 2015, doi:  
682 10.1093/ajh/hpu163.

683 [20] T. Weber *et al.*, “Validation of a Brachial Cuff-Based Method for Estimating Central  
684 Systolic Blood Pressure,” *Hypertension*, vol. 58, no. 5, pp. 825–832, Nov. 2011, doi:  
685 10.1161/HYPERTENSIONAHA.111.176313.

686 [21] A. Tamborini and M. Gharib, “Validation of a Suprasystolic Cuff System for Static and  
687 Dynamic Representation of the Central Pressure Waveform,” *J Am Heart Assoc*, vol. 13,  
688 no. 8, p. e033290, Apr. 2024, doi: 10.1161/JAHA.123.033290.

689 [22] A. Lowe, W. Harrison, E. El-Aklouk, P. Ruygrok, and A. M. Al-Jumaily, “Non-invasive  
690 model-based estimation of aortic pulse pressure using suprasystolic brachial pressure  
691 waveforms,” *J Biomech*, vol. 42, no. 13, pp. 2111–2115, Sep. 2009, doi:  
692 10.1016/j.jbiomech.2009.05.029.

693 [23] V. Fabian *et al.*, “Noninvasive Assessment of Aortic Pulse Wave Velocity by the  
694 Brachial Occlusion-Cuff Technique: Comparative Study,” *Sensors*, vol. 19, no. 16, Art.  
695 no. 16, Jan. 2019, doi: 10.3390/s19163467.

696 [24] J. Sugawara *et al.*, “Brachial–ankle pulse wave velocity: an index of central arterial  
697 stiffness?,” *J Hum Hypertens*, vol. 19, no. 5, pp. 401–406, May 2005, doi:  
698 10.1038/sj.jhh.1001838.

699 [25] J. Sugawara, K. Hayashi, and H. Tanaka, “Distal Shift of Arterial Pressure Wave  
700 Reflection Sites with Aging,” *Hypertension*, vol. 56, no. 5, pp. 920–925, Nov. 2010, doi:  
701 10.1161/HYPERTENSIONAHA.110.160549.

702 [26] S. Munir *et al.*, “Peripheral Augmentation Index Defines the Relationship Between  
703 Central and Peripheral Pulse Pressure,” *Hypertension*, vol. 51, no. 1, pp. 112–118, Jan.  
704 2008, doi: 10.1161/HYPERTENSIONAHA.107.096016.

705 [27] H. Ueda, Y. Nakayama, K. Tsumura, K. Yoshimaru, T. Hayashi, and J. Yoshikawa,  
706 “Inflection Point of Ascending Aortic Waveform Is a Powerful Predictor of Restenosis  
707 After Percutaneous Transluminal Coronary Angioplasty\*,” *American Journal of  
708 Hypertension*, vol. 15, no. 9, pp. 823–826, Sep. 2002, doi: 10.1016/S0895-  
709 7061(02)02981-3.

710 [28] M. Saffarpour *et al.*, “Physiowise: A Physics-aware Approach to Dicrotic Notch  
711 Identification,” *ACM Trans. Comput. Healthcare*, vol. 4, no. 2, p. 10:1-10:17, Apr. 2023,  
712 doi: 10.1145/3578556.

713 [29] R. Pal, A. Rudas, S. Kim, J. N. Chiang, A. Barney, and M. Cannesson, “An algorithm to  
714 detect dicrotic notch in arterial blood pressure and photoplethysmography waveforms  
715 using the iterative envelope mean method,” *Computer Methods and Programs in  
716 Biomedicine*, vol. 254, p. 108283, Sep. 2024, doi: 10.1016/j.cmpb.2024.108283.

717 [30] R. Pal, A. Rudas, T. Williams, J. N. Chiang, A. Barney, and M. Cannesson, “Feature  
718 extraction tool using temporal landmarks in arterial blood pressure and  
719 photoplethysmography waveforms,” *npj Cardiovasc Health*, vol. 2, no. 1, p. 57, Nov.  
720 2025, doi: 10.1038/s44325-025-00096-0.

721 [31] S. A. A. P. Hoeksel, J. R. C. Jansen, J. A. Blom, and J. J. Schreuder, "Detection of  
722 Dicrotic Notch in Arterial Pressure Signals," *J Clin Monit Comput*, vol. 13, no. 5, pp. 309–  
723 316, Sep. 1997, doi: 10.1023/A:1007414906294.

724 [32] A. Tamborini and M. Gharib, "A Pneumatic Low-Pass Filter for High-Fidelity Cuff-  
725 Based Pulse Waveform Acquisition," *Ann Biomed Eng*, vol. 51, no. 11, pp. 2617–2628,  
726 Nov. 2023, doi: 10.1007/s10439-023-03312-z.

727 [33] A. Tamborini and M. Gharib, "Validation of a Suprasystolic Cuff System for Static and  
728 Dynamic Representation of the Central Pressure Waveform," *J Am Heart Assoc*, vol. 13,  
729 no. 8, p. e033290, Apr. 2024, doi: 10.1161/JAHA.123.033290.

730 [34] K. Takazawa, N. Tanaka, K. Takeda, F. Kurosu, and C. Ibukiyama, "Underestimation  
731 of Vasodilator Effects of Nitroglycerin by Upper Limb Blood Pressure," *Hypertension*,  
732 vol. 26, no. 3, pp. 520–523, Sep. 1995, doi: 10.1161/01.HYP.26.3.520.

733 [35] L. Peter, J. Kracik, M. Cerny, N. Noury, and S. Polzer, "Mathematical Model Based on  
734 the Shape of Pulse Waves Measured at a Single Spot for the Non-Invasive Prediction of  
735 Blood Pressure," *Processes*, vol. 8, no. 4, Art. no. 4, Apr. 2020, doi: 10.3390/pr8040442.

736 [36] K. Takazawa *et al.*, "Assessment of Vasoactive Agents and Vascular Aging by the  
737 Second Derivative of Photoplethysmogram Waveform," *Hypertension*, vol. 32, no. 2, pp.  
738 365–370, Aug. 1998, doi: 10.1161/01.HYP.32.2.365.

739 [37] M. Z. Suboh, R. Jaafar, N. A. Nayan, N. H. Harun, and M. S. F. Mohamad, "Analysis on  
740 Four Derivative Waveforms of Photoplethysmogram (PPG) for Fiducial Point Detection,"  
741 *Front. Public Health*, vol. 10, Jun. 2022, doi: 10.3389/fpubh.2022.920946.

742 [38] L. M. Van Bortel *et al.*, "Non-invasive assessment of local arterial pulse pressure:  
743 comparison of applanation tonometry and echo-tracking," *Journal of Hypertension*, vol.  
744 19, no. 6, p. 1037, Jun. 2001.

745 [39] M. C. Kyle and E. D. Freis, "Computer identification of systolic time intervals,"  
746 *Computers and Biomedical Research*, vol. 3, no. 6, pp. 637–651, Dec. 1970, doi:  
747 10.1016/0010-4809(70)90031-5.

748 [40] R. H. Swatzell, W. H. Bancroft, J. Macy, and E. E. Eddleman, "The on-line computer  
749 system for determining the systolic time intervals," *Computers and Biomedical  
750 Research*, vol. 6, no. 5, pp. 465–473, Oct. 1973, doi: 10.1016/0010-4809(73)90079-7.

751 [41] M. J. Oppenheim and D. F. Sittig, "An Innovative Dicrotic Notch Detection Algorithm  
752 Which Combines Rule-Based Logic with Digital Signal Processing Techniques,"  
753 *Computers and Biomedical Research*, vol. 28, no. 2, pp. 154–170, Apr. 1995, doi:  
754 10.1006/cbmr.1995.1011.

755 [42] L. Peter, N. Noury, M. Cerny, and I. Nykl, "Comparison of methods for the evaluation  
756 of NIBP from pulse transit time," in *2016 38th Annual International Conference of the  
757 IEEE Engineering in Medicine and Biology Society (EMBC)*, Aug. 2016, pp. 4244–4247.  
758 doi: 10.1109/EMBC.2016.7591664.

759 [43] P. S. Nandi and D. H. Spodick, "Determination of systolic intervals utilizing the  
760 carotid first derivative," *American Heart Journal*, vol. 86, no. 4, pp. 495–500, Oct. 1973,  
761 doi: 10.1016/0002-8703(73)90141-5.

762 [44] A. Aghilinejad, A. Tamborini, and M. Gharib, "A new methodology for determining the  
763 central pressure waveform from peripheral measurement using Fourier-based machine

764 learning," *Artificial Intelligence in Medicine*, p. 102918, Jun. 2024, doi:  
765 10.1016/j.artmed.2024.102918.

766 [45] A. Aghilinejad and M. Gharib, "Assessing pressure wave components for aortic  
767 stiffness monitoring through spectral regression learning," *European Heart Journal  
768 Open*, vol. 4, no. 3, p. oeae040, May 2024, doi: 10.1093/ehjopen/oeae040.

769 [46] J. P. Murgo, N. Westerhof, J. P. Giolma, and S. A. Altobelli, "Aortic input impedance in  
770 normal man: relationship to pressure wave forms," *Circulation*, vol. 62, no. 1, pp. 105–  
771 116, Jul. 1980, doi: 10.1161/01.CIR.62.1.105.

772 [47] M. F. O'Rourke and D. E. Gallagher, "Pulse wave analysis," *J Hypertens Suppl*, vol.  
773 14, no. 5, pp. S147–157, Dec. 1996.

774 [48] I. B. Wilkinson *et al.*, "Reproducibility of pulse wave velocity and augmentation index  
775 measured by pulse wave analysis," *Journal of Hypertension*, vol. 16, no. 12, p. 2079,  
776 Dec. 1998.

777 [49] A. Tamborini, A. Aghilinejad, and M. Gharib, "Abstract 4141635: Reconstructing  
778 Invasive Aortic Pressure Waveforms from Non-Invasive Brachial Measurements Using a  
779 Machine Learning Approach," *Circulation*, vol. 150, no. Suppl\_1, pp. A4141635–  
780 A4141635, Nov. 2024, doi: 10.1161/circ.150.suppl\_1.4141635.

781 [50] A. Aghilinejad, A. Tamborini, and M. Gharib, "Abstract 4142004: Predicting  
782 Cardiovascular Disease Events Using Uncalibrated Non-invasive Carotid Pressure  
783 Wave Components from Spectral Regression Learning," *Circulation*, vol. 150, no.  
784 Suppl\_1, pp. A4142004–A4142004, Nov. 2024, doi: 10.1161/circ.150.suppl\_1.4142004.

785 [51] W. W. Nichols, "Clinical measurement of arterial stiffness obtained from  
786 noninvasive pressure waveforms," *American Journal of Hypertension*, vol. 18, no. S1,  
787 pp. 3S–10S, Jan. 2005, doi: 10.1016/j.amjhyper.2004.10.009.

788 [52] J. J. Oliver and D. J. Webb, "Noninvasive Assessment of Arterial Stiffness and Risk of  
789 Atherosclerotic Events," *Arteriosclerosis, Thrombosis, and Vascular Biology*, vol. 23, no.  
790 4, pp. 554–566, Apr. 2003, doi: 10.1161/01.ATV.0000060460.52916.D6.

791 [53] S. Meaume, A. Benetos, O. F. Henry, A. Rudnichi, and M. E. Safar, "Aortic Pulse Wave  
792 Velocity Predicts Cardiovascular Mortality in Subjects >70 Years of Age,"  
793 *Arteriosclerosis, Thrombosis, and Vascular Biology*, vol. 21, no. 12, pp. 2046–2050, Dec.  
794 2001, doi: 10.1161/hq1201.100226.

795 [54] A. Aghilinejad, A. Tamborini, and M. Gharib, "Decoding vascular age from brachial  
796 waveform morphology via machine learning and model-based data augmentation,"  
797 *Mach. Learn.: Health*, vol. 1, no. 1, p. 015006, Dec. 2025, doi: 10.1088/3049-  
798 477X/adf74f.

799 [55] W. W. Nichols and D. G. Edwards, "Arterial Elastance and Wave Reflection  
800 Augmentation of Systolic Blood Pressure: deleterious Effects and Implications for  
801 Therapy," *J Cardiovasc Pharmacol Ther*, vol. 6, no. 1, pp. 5–21, Mar. 2001, doi:  
802 10.1177/107424840100600102.

803 [56] Y.-L. Zhang, Y.-Y. Zheng, Z.-C. Ma, and Y.-N. Sun, "Radial pulse transit time is an  
804 index of arterial stiffness," *Hypertens Res*, vol. 34, no. 7, pp. 884–887, Jul. 2011, doi:  
805 10.1038/hr.2011.41.

806 [57] M. F. O'Rourke and A. L. Pauca, "Augmentation of the aortic and central arterial  
807 pressure waveform," *Blood Pressure Monitoring*, vol. 9, no. 4, p. 179, Aug. 2004.

808 [58] P. S. Lacy, D. G. O'Brien, A. G. Stanley, M. M. Dewar, P. P. Swales, and B. Williams,  
809       “Increased pulse wave velocity is not associated with elevated augmentation index in  
810       patients with diabetes,” *Journal of Hypertension*, vol. 22, no. 10, p. 1937, Oct. 2004.  
811 [59] A. Hughes *et al.*, “Limitations of Augmentation Index in the Assessment of Wave  
812       Reflection in Normotensive Healthy Individuals,” *PLoS one*, vol. 8, p. e59371, Mar. 2013,  
813       doi: 10.1371/journal.pone.0059371.  
814 [60] F. Fantin, A. Mattocks, C. J. Bulpitt, W. Banya, and C. Rajkumar, “Is augmentation  
815       index a good measure of vascular stiffness in the elderly?,” *Age Ageing*, vol. 36, no. 1,  
816       pp. 43–48, Jan. 2007, doi: 10.1093/ageing/afl115.  
817

Variable	Quantity (n=145)
<b>Age</b> , years	66 ± 9
<b>Height</b> , cm	170 ± 10
<b>Weight</b> , kg	84.6 ± 19.2
<b>BMI</b> , kg/m <sup>2</sup>	29.0 ± 5.5
<b>Male</b> , n (%)	88 (61%)
<b>White</b> , n (%)	96 (66%)
<b>Smoker</b> , n (%)	22 (15%)
<b>Diabetes</b> , n (%)	51 (35%)
<b>Hypertension</b> , n (%)	115 (79%)
<b>Hyperlipidemia</b> , n (%)	107 (74%)

820 **Table 1** – Study population characteristics.

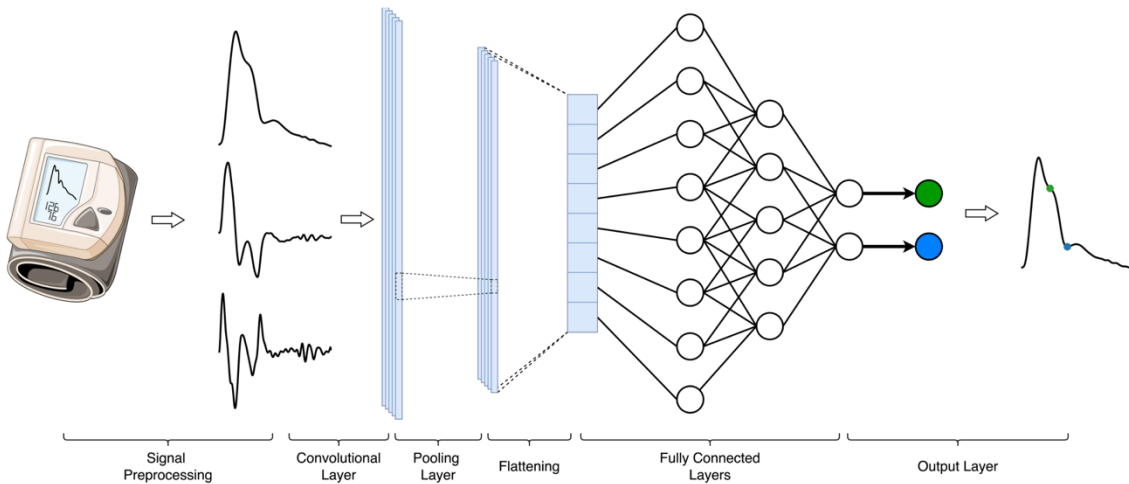
		Experiment Number								
		1	2	3	4	5	6	7	8	9
Metric										
	<b>r</b>	0.85	0.88	0.86	0.92	0.86	0.91	0.89	0.91	0.89
	<b>R<sup>2</sup></b>	0.71	0.77	0.74	0.85	0.74	0.83	0.79	0.82	0.79
<i>t<sub>i</sub></i>	<b>RMSE, ms</b>	29	25	27	21	27	22	24	22	24
	<b>Mean Difference, ms</b>	-7	-2	2	0	2	0	0	-1	-2
	<b>Limits of Agreement, ms</b>	54	49	53	41	52	42	47	44	47
	<b>r</b>	0.89	0.91	0.90	0.89	0.91	0.94	0.92	0.92	0.89
	<b>R<sup>2</sup></b>	0.77	0.82	0.78	0.78	0.81	0.88	0.85	0.83	0.76
<i>t<sub>n</sub></i>	<b>RMSE, ms</b>	19	17	18	18	17	14	15	16	19
	<b>Mean Difference, ms</b>	4	3	6	1	2	0	1	0	3
	<b>Limits of Agreement, ms</b>	37	32	34	36	33	27	30	32	37

822 **Table 2** – Prediction accuracy metrics for the cardiac wave fiducial point predictions for the  
 823 hyperparameter and algorithm tuning experiments.

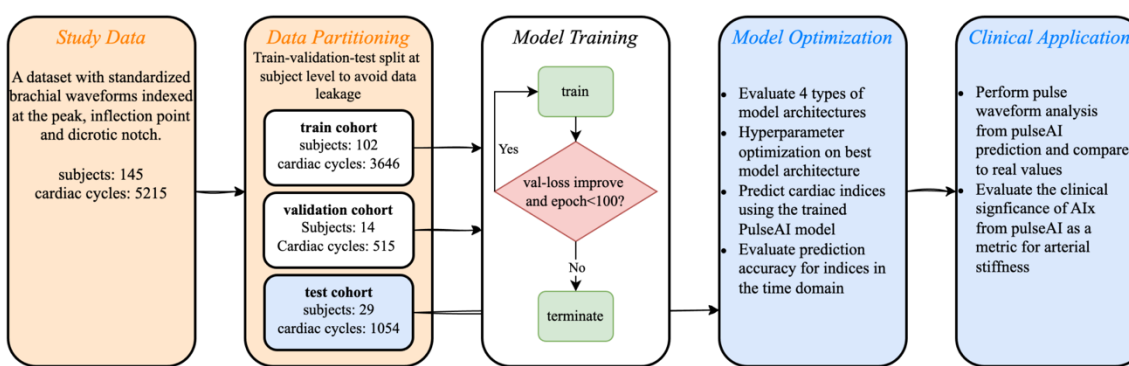
824

825

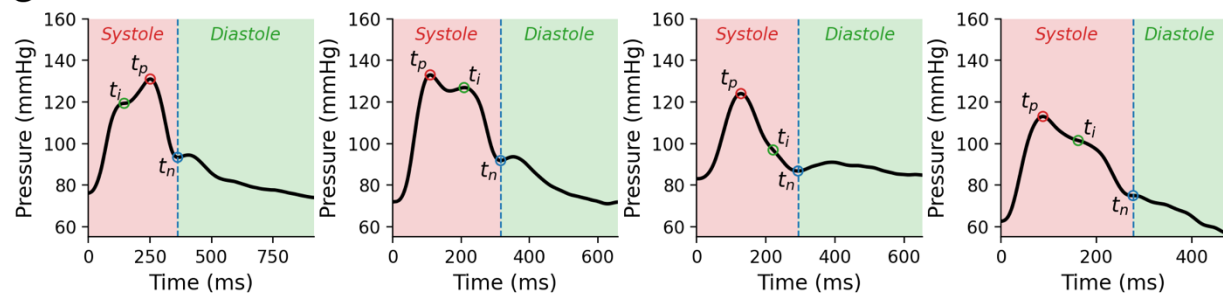
A

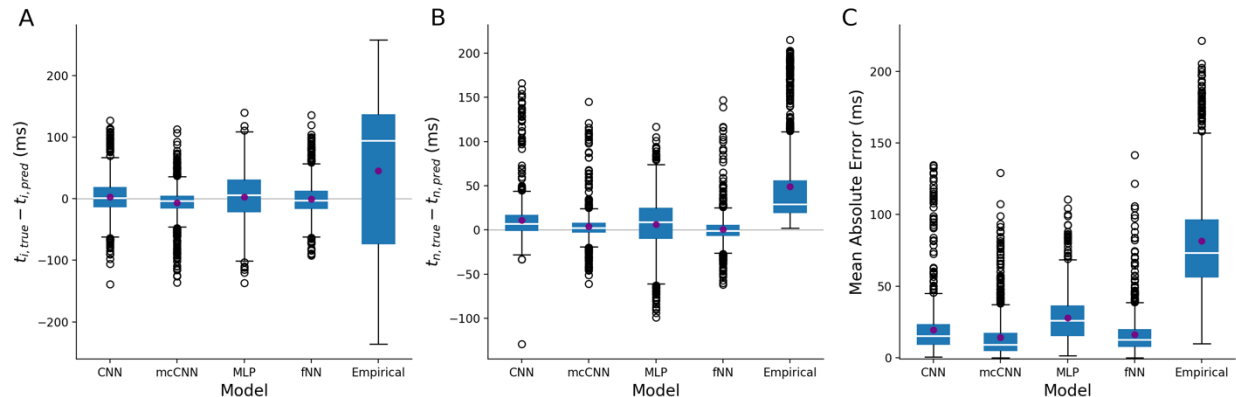


B

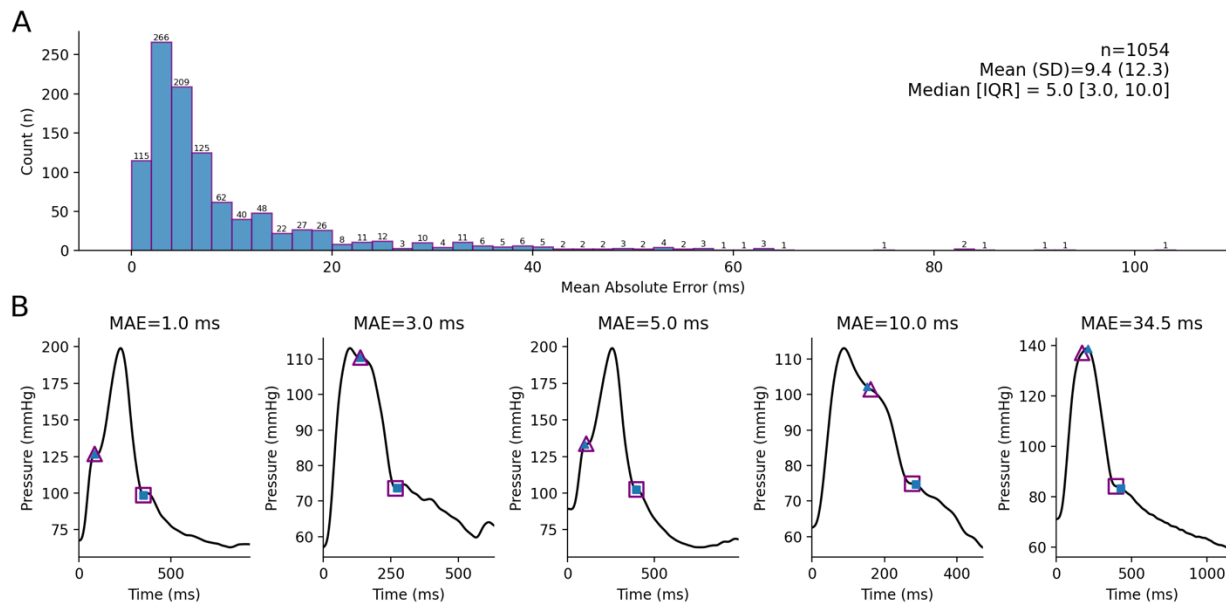


C



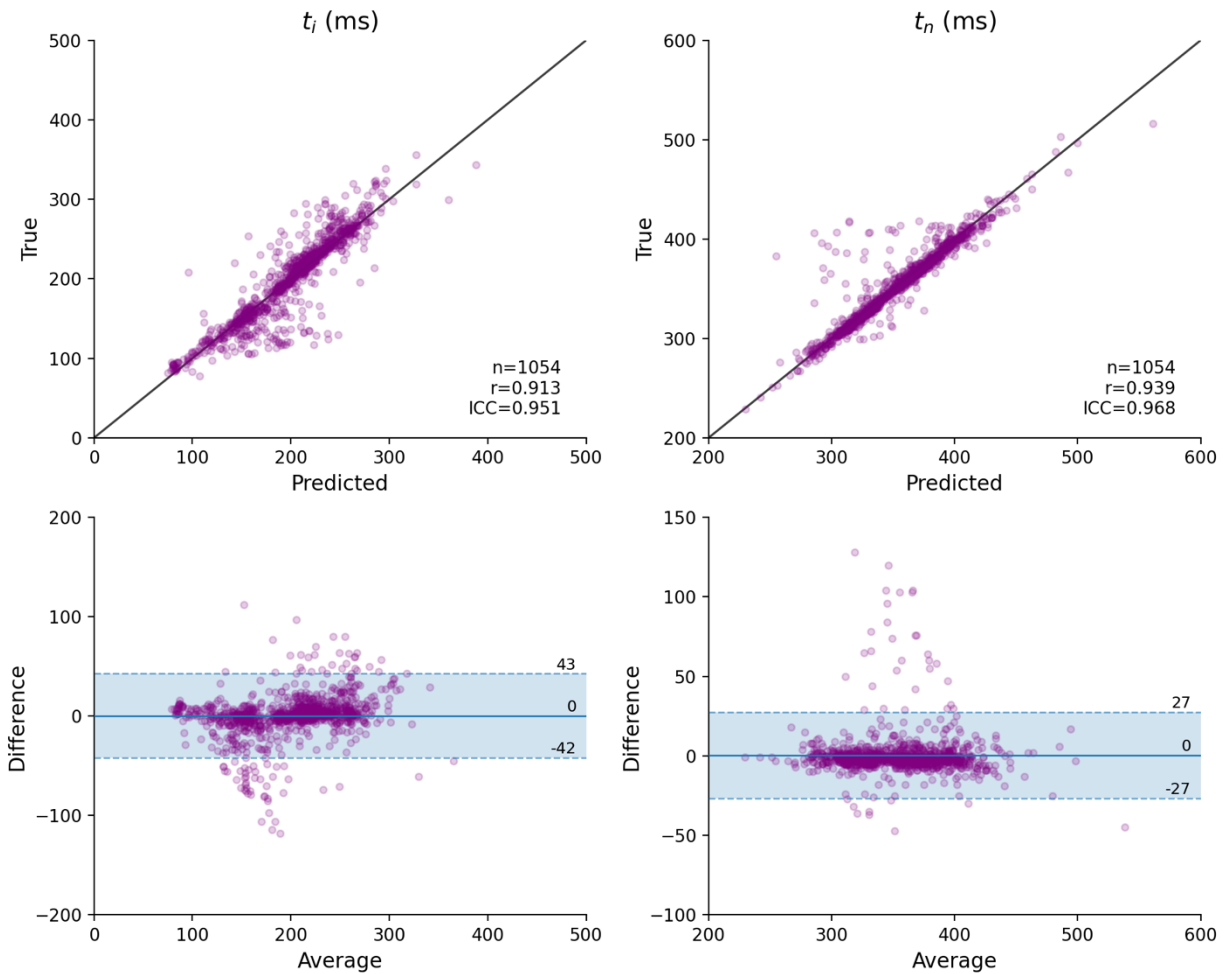


836  
837 **Figure 2 – Fiducial point prediction errors across different model architectures.** (A) and  
838 (B) show the prediction error (true – predicted) for the inflection point,  $t_i$ , and the dicrotic  
839 notch,  $t_n$ , respectively. (C) Displays the mean absolute error (MAE) for fiducial point  
840 detection across various algorithms, including the convolutional neural network (CNN),  
841 multi-channel CNN (mcCNN), multi-layer perceptron (MLP), Fourier-based neural network  
842 (fNN), and the empirical model.  
843

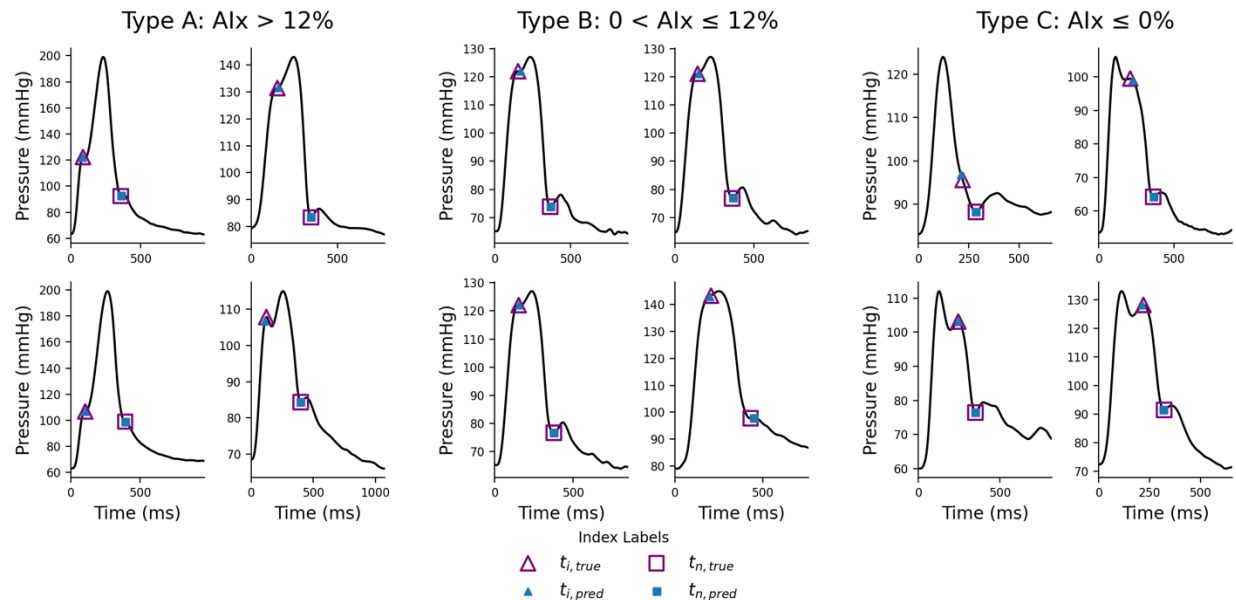


844  
845  
846  
847  
848  
849

**Figure 3 – Performance of the optimized PulseAI model error in the test population. (A)**  
 Mean absolute error (MAE) distribution across the test population (n=1,054). (B) Five sample  
 waveforms illustrating fiducial point predictions across the error spectrum at the 5<sup>th</sup>, 25<sup>th</sup>,  
 50<sup>th</sup>, 75<sup>th</sup> and 95<sup>th</sup> percentile of MAE.

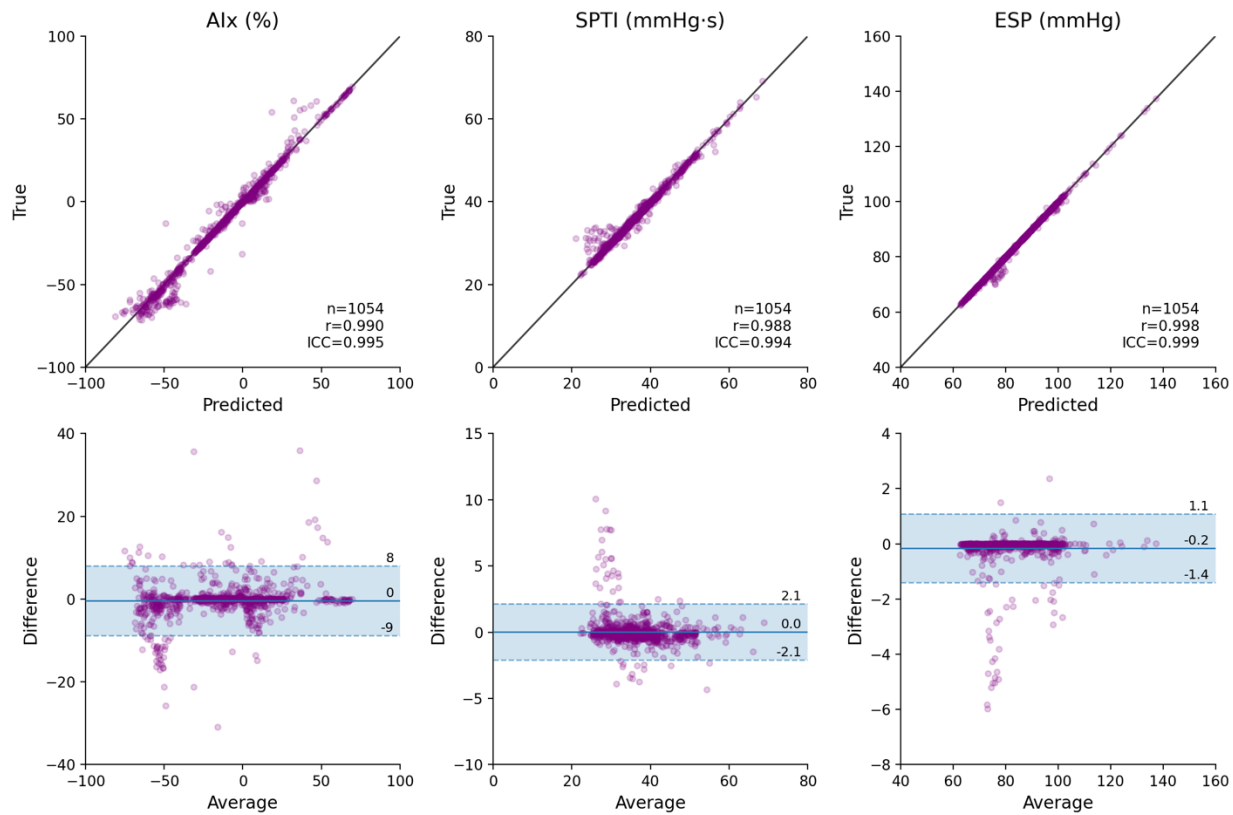


850  
851 **Figure 4 – Prediction accuracy of PulseAI for pulse waveform fiducial points.** (Top) True-  
852 versus-predicted plots for fiducial points  $t_i$  and  $t_n$ , with the black solid line representing the  
853 line of proportionality. (Bottom) Bland-Altman plots for  $t_i$  and  $t_n$  where the solid blue line  
854 indicates the mean difference, and the shaded area represents the limits of agreement.  
855  
856  
857



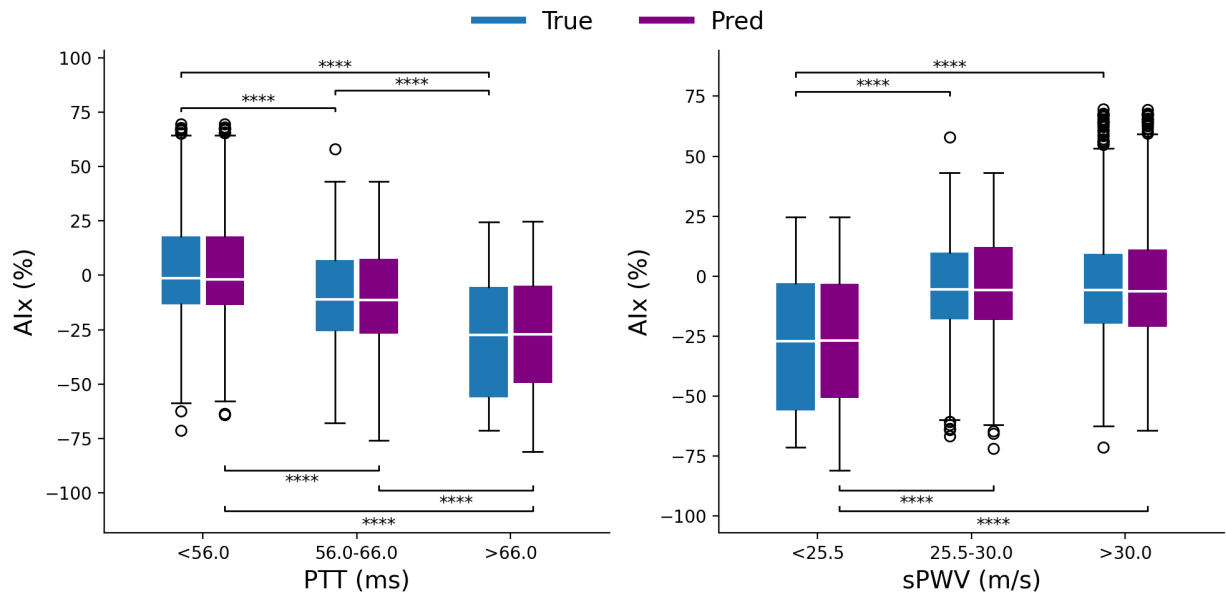
858  
859  
860  
861  
862

**Figure 5 – PulseAI fiducial point predictions versus true measurement across different wave morphologies.** True and predicted fiducial points are shown for waveforms classified based on the shape type according to Augmentation Index (Alx) morphology definitions.



863  
864  
865  
866  
867  
868  
869  
870  
871

**Figure 6 – Evaluation of pulse waveform analysis (PWA) accuracy using PulseAI-predicted fiducial points.** (Top) True-versus-predicted plots for pulse waveform features extracted via PWA using true and predicted fiducial points. From left to right, the features include Augmentation Index (Alx), systolic pressure-time integral (SPTI), and end-systolic pressure (ESP). The black solid line represents the proportionality line. (Bottom) Bland-Altman plots for the PWA features, with the solid blue line denoting the mean difference, and the shaded area representing the limits of agreement.



872  
873  
874  
875  
876  
877

**Figure 7 – Relationship between arterial stiffness and PulseAI-derived Augmentation Index (Alx).** Alx measurements are compared with pulse transit time (PTT) and surrogate of pulse wave velocity (sPWV) as indirect measures of arterial stiffness. Statistical significance is marked as \* p<0.05, \*\* p<0.01, \*\*\* p<0.001, \*\*\*\* p<0.0001.